nature COMMUNICATIONS

ARTICLE

Received 6 Nov 2013 | Accepted 14 Feb 2014 | Published 27 Mar 2014

DOI: 10.1038/ncomms4453 OPEN

Elastic anisotropy of experimental analogues of perovskite and post-perovskite help to interpret D″ diversity

Akira Yoneda[1], Hiroshi Fukui[2,3], Fang Xu[1], Akihiko Nakatsuka[4], Akira Yoshiasa[5], Yusuke Seto[6], Kenya Ono[7], Satoshi Tsutsui[8], Hiroshi Uchiyama[8] & Alfred Q. R. Baron[3,8]

Recent studies show that the D″ layer, just above the Earth's core–mantle boundary, is composed of $MgSiO_3$ post-perovskite and has significant lateral inhomogeneity. Here we consider the D″ diversity as related to the single-crystal elasticity of the post-perovskite phase. We measure the single-crystal elasticity of the perovskite *Pbnm*-$CaIrO_3$ and post-perovskite *Cmcm*-$CaIrO_3$ using inelastic X-ray scattering. These materials are structural analogues to same phases of $MgSiO_3$. Our results show that *Cmcm*-$CaIrO_3$ is much more elastically anisotropic than *Pbnm*-$CaIrO_3$, which offers an explanation for the enigmatic seismic wave velocity jump at the D″ discontinuity. Considering the relation between lattice preferred orientation and seismic anisotropy in the D″ layer, we suggest that the *c* axis of post-perovskite $MgSiO_3$ aligns vertically beneath the Circum-Pacific rim, and the *b* axis vertically beneath the Central Pacific.

[1] Institute for Study of the Earth's Interior, Okayama University, Misasa, Tottori 682-0193, Japan. [2] Graduate School of Material Science, University of Hyogo, Kamigori, Hyogo 678-1297, Japan. [3] Materials Dynamics Laboratory, RIKEN SPring-8 Center, RIKEN, Hyogo 679-5148, Japan. [4] Graduate School of Science and Engineering, Yamaguchi University, Ube, Yamaguchi 755-8611, Japan. [5] Graduate School of Science and Technology, Kumamoto University, Kumamoto 860-8555, Japan. [6] Graduate School of Science, Kobe University, Kobe 657-8501, Japan. [7] Department of Earth Sciences, University of Toyama, Toyama 930-8555, Japan. [8] Japan Synchrotron Radiation Research Institute, SPring-8, Sayo, Hyogo 679-5198, Japan. Correspondence and requests for materials should be addressed to A.Y. (email: yoneda@misasa.okayama-u.ac.jp).

Since the discovery of the transition from perovskite (Pv) to post-perovskite (pPv) in $MgSiO_3$ (refs 1,2), pPv-$MgSiO_3$ has been considered to be a major component of the D″ layer just above the core–mantle boundary (CMB). Seismological observations of the D″ layer are difficult to interpret as they suggest both non-uniform response at the layer boundary and non-uniform anisotropy inside the layer[3–5]. With this background, elastic anisotropy or single-crystal elasticity of pPv-$MgSiO_3$ has been the focus of theoretical calculations[6–10]. However, no experimental data are available on the single-crystal elasticity of pPv-$MgSiO_3$, because it is unstable at ambient pressure.

Cmcm-$CaIrO_3$ or pPv-$CaIrO_3$ has been frequently selected as a representative analogue of pPv-$MgSiO_3$ (refs 11–13). According to the phase diagram[14], pPv-$CaIrO_3$ is the stable phase at ambient conditions and Pv-$CaIrO_3$ is the high-temperature and low-pressure phase. Here we report the first experimental data on single-crystal elasticity of Pv and pPv structures in a homogeneous chemical composition of $CaIrO_3$.

Results

Characterization of single-crystal specimen. Figure 1a,b shows single crystals of Pv-$CaIrO_3$ and pPv-$CaIrO_3$ used in the present study. The Pv-$CaIrO_3$ sample was synthesized at 2 GPa and 1,450 °C for 15 h in a piston cylinder apparatus at Okayama University. We produced many grains with size of a few tens of microns, although most of them turned out to have multiple domains. We examined more than 20 grains using a four-circle X-ray diffractometer at Yamaguchi University and selected a quasi-single-domain crystal with size of ~20 μm. Its lattice constants were determined as $a = 5.3527(1)$, $b = 5.5969(5)$ and $c = 7.6804(6)$ Å, which yields density (ρ) of 8,091 kg m^{-3}. The pPv-$CaIrO_3$ sample was synthesized by slow cooling from 1,000 °C in $CaCl_2$ flux[15]. It had a pine-needle shape with length of a few 100 microns and width of a few 10s of microns. Its lattice constant and densities were respectively $a = 3.145(2)$, $b = 9.861(6)$, and $c = 7.297(5)$ Å, and ρ = 8,211 kg m^{-3}, which are consistent with literature values[16].

Inelastic X-ray scattering measurement and results. Figure 1c,d compare experimental velocities obtained from the inelastic X-ray scattering (IXS) spectra with velocities calculated from the optimized elastic constants. The details of the IXS measurement are described in the Methods section for the measurement of IXS at SPring-8 BL35XU; one of the important advantages of IXS compared with Brillouin scattering is its geometrical freedom (see Supplementary Methods). The analytical procedures for determining single-crystal elastic constants are described in the Methods section for data analysis for elastic constants. The measurement data are summarized in Supplementary Tables 1 and 2.

Table 1 summarizes the results of elastic constants and gives isotropic averages. The values are reasonably consistent with the theoretical results[17] except for a few discrepancies. The high-pressure phase of pPv-$CaIrO_3$ is less compressible than Pv-$CaIrO_3$ whereas the theoretical prediction suggests the opposite relation. In addition, isotropic averages of V_P and V_S are significantly larger for pPv-$CaIrO_3$ than for Pv-$CaIrO_3$ according to the present results. Figure 2 compares the present results and theoretical calculations for the velocity surfaces of Pv-$CaIrO_3$ and pPv-$CaIrO_3$. We see fairly good agreement between the two results for pPv-$CaIrO_3$, although we recognize significant differences between them for Pv-$CaIrO_3$. Figure 3 shows the compatibility of the elastic constants with compression data[18]. The present data are consistent with the compression data for Pv- and pPv-$CaIrO_3$; the theoretical result for Pv-$CaIrO_3$, however, yields a different slope from the others.

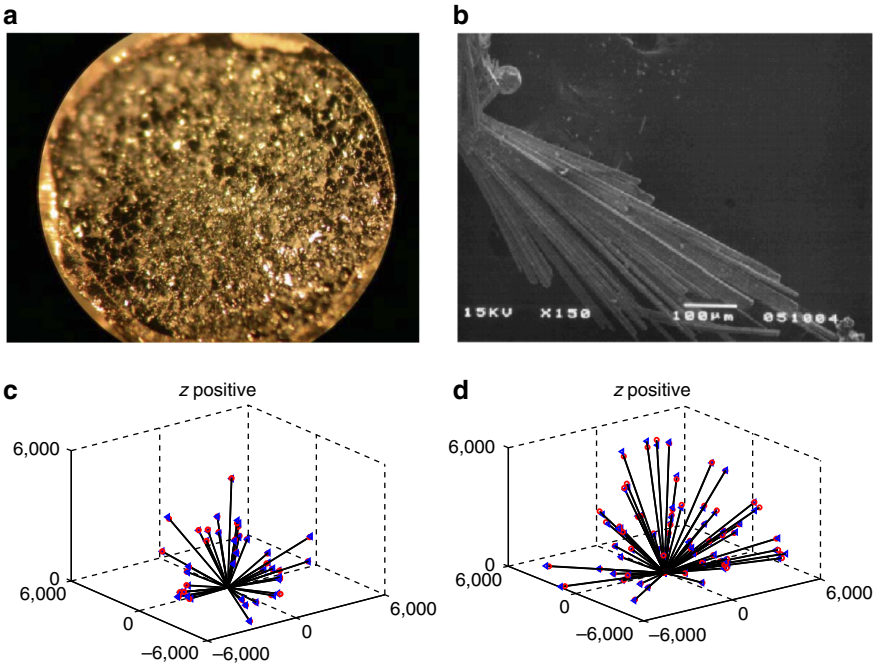

Figure 1 | Specimen and measurement data. Left and right columns refer to *Pbnm*- and *Cmcm*-$CaIrO_3$, respectively. (**a**,**b**) Photographs of single crystals used. The horizontal edge lengths are ~5 mm and ~800 μm, respectively, for **a** and **b**. (**c**,**d**) Overall picture for the experimental data and analytical fitting. Black lines indicate the direction of wave propagation in the crystal, and blue triangles and red circles are experimental velocities and recalculated values after least-squares analysis. The vertical direction is positive *z* direction, while horizontal leftward and rightward directions are positive *x* and *y* directions, respectively. Note that the difference between experimental and recalculated velocities is less than 5%. The misfit uniformly distributed indicates untwinned crystal specimens.

Table 1 | Single-crystal elastic moduli of *Pbnm*- and *Cmcm*-$CaIrO_3$.

	C_{11}	C_{22}	C_{33}	C_{12}	C_{23}	C_{31}	C_{44}	C_{55}	C_{66}	K_R	K_H	G_H	V_P	V_S
Pbnm (Pv)	235 (6)	278 (6)	286 (11)	132 (6)	138 (11)	120 (10)	87 (4)	60 (2)	79 (2)	173 (6)	174 (6)	72 (2)	5,776 (54)	2,976 (42)
	248	359	319	204	162	115	79	42	97	195	202	68	6,001	2,892
Cmcm (pPv)	378 (4)	255 (11)	360 (5)	104 (7)	137 (9)	73 (6)	76 (5)	56 (2)	85 (3)	178 (4)	179 (4)	84 (1)	5,955 (46)	3,201 (27)
	388	241	386	121	149	85	67	46	64	186	189	98	5,913	2,990

Several isotropic moduli and velocities are shown on the right-hand side. The upper two rows are for *Pbnm* or Pv structure, while the lower two rows are for *Cmcm* or pPv structure. In each case, the first row gives the present experimental results with accuracy and the second row the theoretical results obtained by Tsuchiya and Tsuchiya[17]. The unit is 'GPa' except for velocities which have a unit of '$m\,s^{-1}$' in the last two columns. The numbers in parentheses correspond to fitting error in the least square analysis.

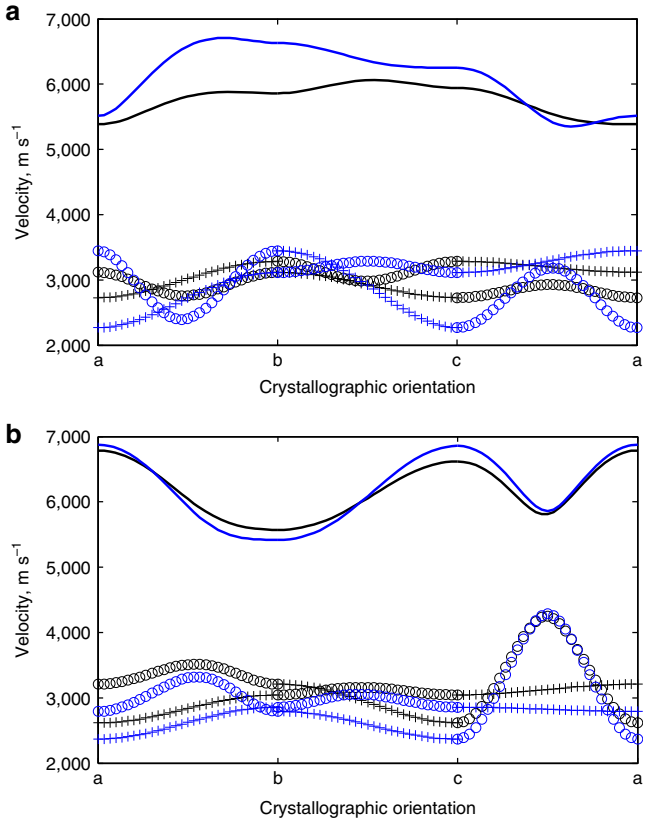

Figure 2 | Velocity surface of *Pbnm*- and *Cmcm*-$CaIrO_3$. Upper (**a**) and lower (**b**) plots correspond to *Pbnm*- and *Cmcm*-$CaIrO_3$, respectively. Black lines are drawn for the present results, while blue lines are drawn for the results obtained by Tsuchiya and Tsuchiya[17]. Upper lines correspond to the P-wave velocity, and lower lines to the S-wave velocity. Open circles 'o' and crosses '+' for V_S specify in-plane and out-of-plane particle motions.

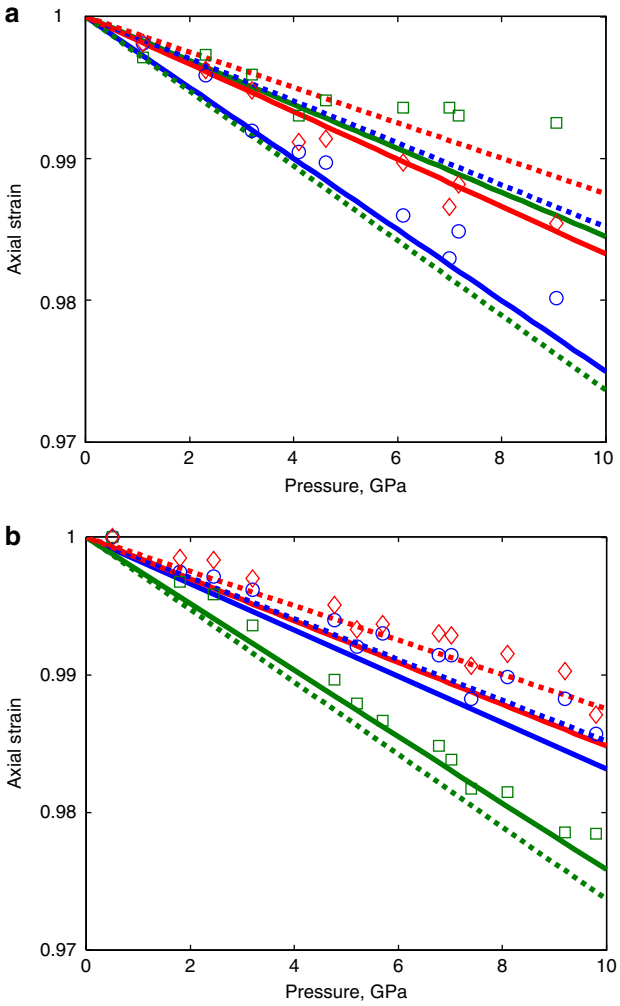

Figure 3 | Comparison of compression curves. Upper (**a**) and lower (**b**) plots correspond to *Pbnm*- and *Cmcm*-$CaIrO_3$, respectively. The lattice constants *a*, *b*, and *c* are shown in blue, green and red respectively. Solid and dotted lines are drawn for the present data and Tsuchiya's theoretical data[17], respectively, while symbols are the compression data.

Discussion

Figure 4 presents stereo projections of elastic wave velocities for Pv and pPv structures of $CaIrO_3$. It shows that the ranges of variation of V_P, the average of V_S values, and the difference in V_S values are $\sim$600, $\sim$300 and $\sim$500 $m\,s^{-1}$ for Pv-$CaIrO_3$ and $\sim$1,000, $\sim$800 and $\sim$1,100 $m\,s^{-1}$, for pPv-$CaIrO_3$, respectively. We see that pPv-$CaIrO_3$ has approximately double the anisotropy of Pv-$CaIrO_3$ in terms of the elastic wave velocity. For example, anisotropy in the polarization shear wave velocity is $\sim$30% in pPv-$CaIrO_3$ while it is only $\sim$15% in Pv-$CaIrO_3$.

From Fig. 4d,e for pPv phase, the *b* axis is found to be the direction of the lowest V_P, while the highest *Vs* is between the *a* and *c* axes. These pronounced features of the pPv elasticity are understandable as alternate stacking of compliant and stiff layers perpendicular to the *b* axis; the stiff layer has the largest shear wave constant and lowest longitudinal wave constant between *a* and *c* axes. We recognize similarity between *a* and *c* axes in pPv-$CaIrO_3$ elasticity, while the *a* axis is slightly stiffer than the *c* axis in terms of both longitudinal and shear wave

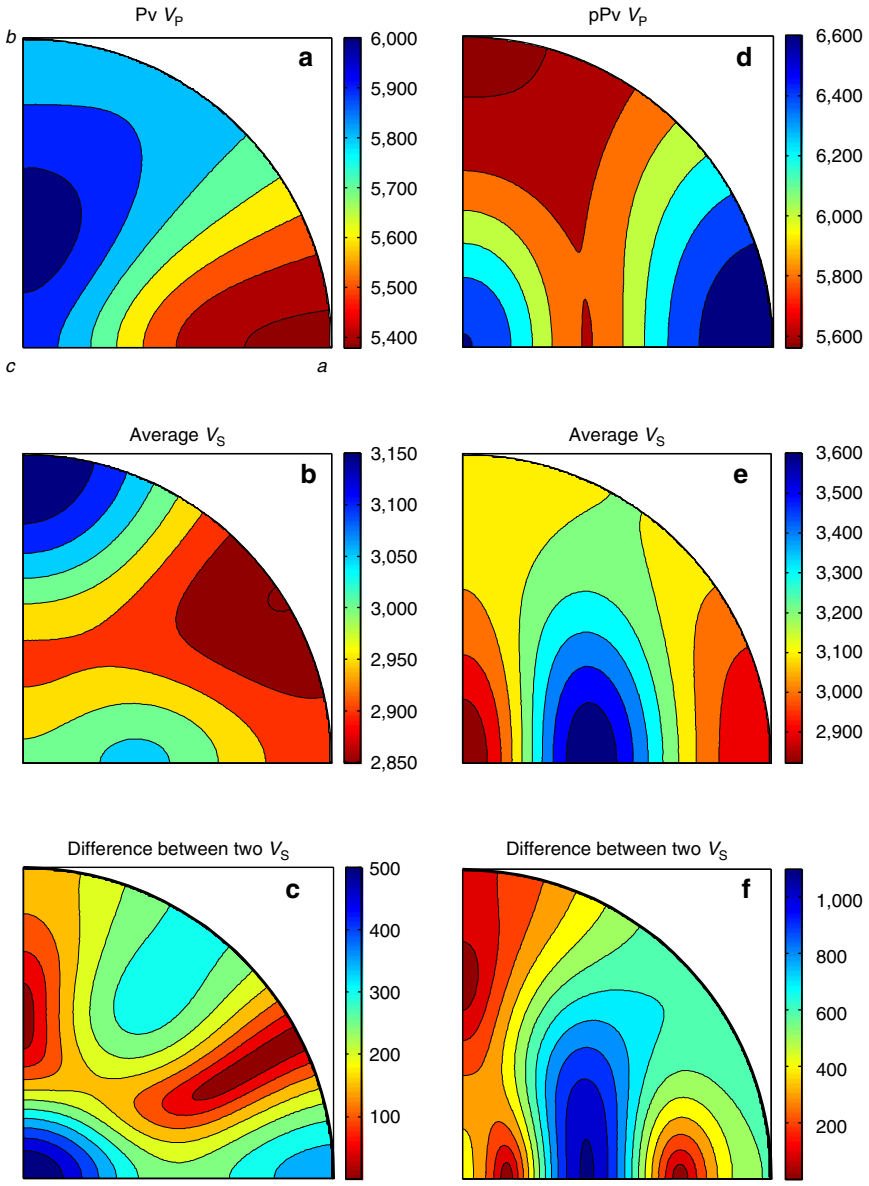

Figure 4 | Velocity surface of Pv- and pPv-$CaIrO_3$. Stereo projections of elastic wave velocities for Pv- and pPv-$CaIrO_3$ based on the present results. The crystallographic directions, *a*, *b*, and, *c*, are identical in each plot as shown in (**a**). The unit of scale bars is m s^{-1}. (**a**–**c**) V_P, average of two V_S values, and difference between two V_S values, respectively, for Pv-$CaIrO_3$. (**d**–**f**) Same as **a**, **b**, and **c** but for pPv-$CaIrO_3$.

constants. The elasticity of Pv-$CaIrO_3$ resembles that of Pv-$MgSiO_3$ under lower-mantle conditions more than under ambient conditions (Fig. 5). Elasticity of Pv- and pPv-$CaIrO_3$ under ambient conditions seems to be a good indicator of that of Pv- and pPv-$MgSiO_3$ under lowermost mantle conditions; a conversion factor of 2.2–2.4 is found between them.

We interpret the D″ diversity observed seismologically in terms of the single-crystal elasticity of Pv and pPv-$CaIrO_3$. Significant anisotropy of the seismic wave velocity has been observed in the D″ layer, while the lower mantle above the D″ layer is nearly isotropic with a high degree of confidence[19]. Therefore, we plotted the velocity difference between anisotropic pPv and isotropic Pv both for $CaIrO_3$ under ambient conditions and $MgSiO_3$ under mantle conditions (Fig. 6). From the plots for V_P and slower V_S, we see that any velocity change over the D″ discontinuity is possible both for P and S waves depending on the lattice preferred orientation (LPO) characteristics of the pPv phase.

The seismic wave phases used in the D″ study (S, ScS, Sdiff) travel nearly horizontally in the D″ layer[4]. Therefore, the two polarized S waves are classified as SH and SV, whose polarizations are in the horizontal and vertical directions, respectively. In seismological study, vertically transverse isotropy (VTI) and the tilted transverse isotropy have been assumed to explain S-wave polarization anisotropy in the D″ layer[4].

According to seismological studies, the region of the Circum-Pacific rim is interpreted as having VTI with $V_{SH} > V_{SV}$, while the region of the Central Pacific has complicated VTI without any fixed relation between V_{SH} and V_{SV}[4]. Polarization anisotropy is not recognized beneath the Atlantic Ocean, or the region is considered as having VTI with $V_{SH} \approx V_{SV}$. On the other hand, from the polarization pattern in the *a*–*b* plane of the faster V_S plot (Figs 2b and 7), we can expect that $V_{SH} > V_{SV}$ in the D″ layer if the *c* axis of pPv aligns vertically. Similarly, if the *b* axis aligns vertically, the magnitude relation between V_{SH} and V_{SV} can be complicated.

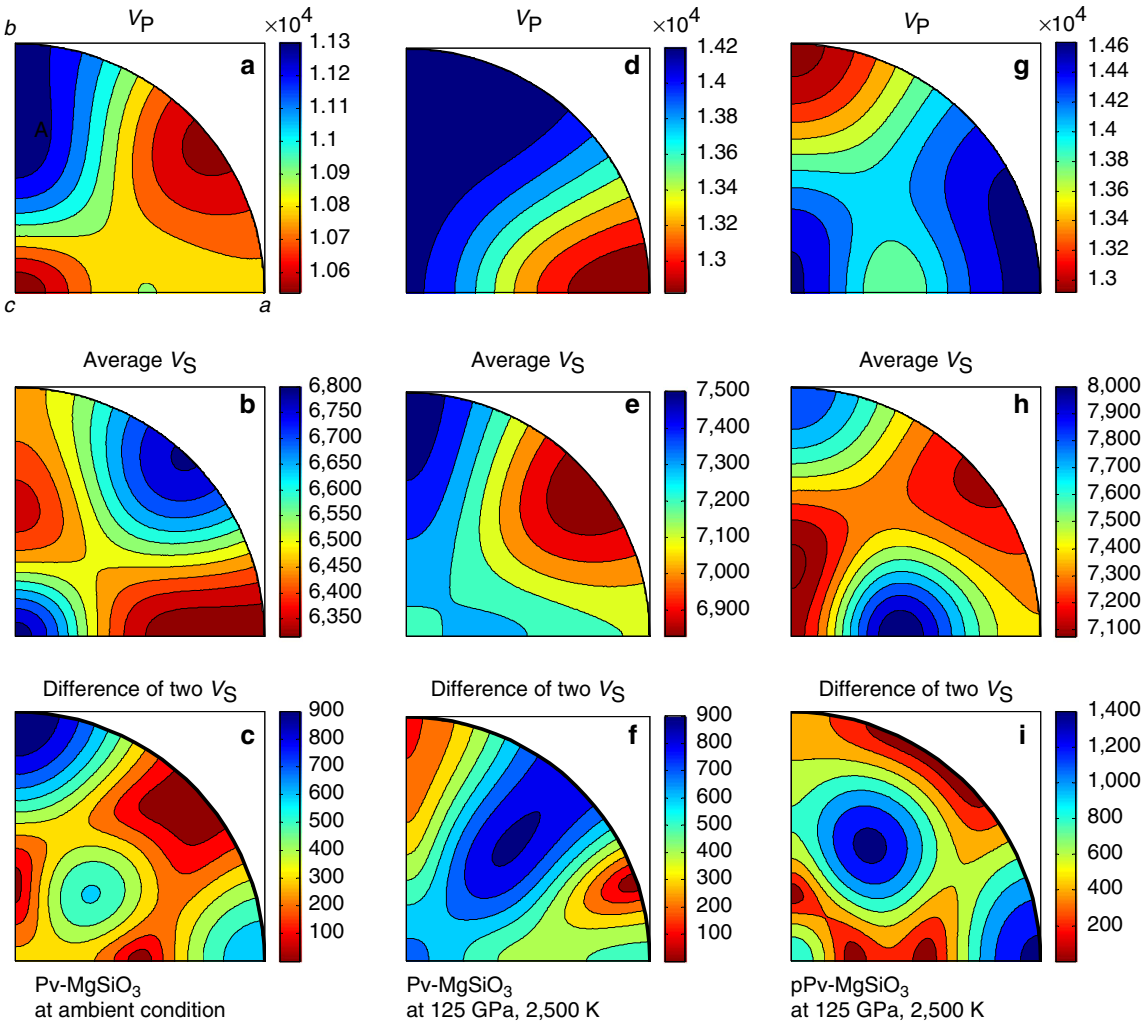

Figure 5 | Stereo projections of elastic wave velocities for Pv- and pPv-$MgSiO_3$. The crystallographic directions, *a*, *b*, and, *c*, are identical in each plot as shown in (**a**). The unit of scale bars is m s^{-1}, although a factor of 10^4 should be multiplied for V_P. (**a**–**c**) V_P, average of two V_S values, and difference between two V_S values, respectively, for Pv-$MgSiO_3$ under ambient conditions. (**d**–**f**) and (**g**–**i**) Same as **a**, **b**, and **c** but for Pv-$MgSiO_3$ and pPv-$MgSiO_3$ at 125 GPa and 2,500 K[10], respectively.

We can summarize the above conclusion in an alternative way: For the *c* axis vertical case, horizontal wave propagation directions lie in the a–b plane, for which the in-plane shear mode (SH) has consistently higher wave speeds (Figs 2b and 7). If instead the *b* axis is vertical, horizontal wave propagation directions lie in the a–c plane, for which neither the in-plane (SH) nor the out-of-plane (SV) is consistently faster for all such propagation directions (Figs 2b and 7).

The dominant slip system of pPv-$CaIrO_3$ was determined as [100](010) from shear deformation experiments[11]. Since the slip system of pPv-$MgSiO_3$ has not yet been determined, we assumed that it is similar to that of pPv-$CaIrO_3$[11]. This assumption leads to LPO of pPv-$MgSiO_3$, in which the *b* axis aligns vertically along the lateral flow in the D″ layer. The LPO pattern is consistent with the complicated polarization S-wave anisotropy beneath the Central Pacific (Figs 2b and 7).

Although the texture development during Pv–pPv transition in $MgSiO_3$ has not yet been clarified, we expect the *c* axis alignment of pPv-$MgSiO_3$ immediately after the phase transition from Pv-$MgSiO_3$ from analogy with the case for $MgGeO_3$ (ref. 20). If the *c* axis aligns vertically, we expect VTI with $V_{SH} > V_{SV}$, which is consistent with the seismic feature beneath the Circum-Pacific rim.

Employing this conceptual scheme, we evaluated the feasibility of the LPO model of pPv in the D″ layer. The volume ratio between (Mg, Fe)SiO_3 Pv and (Mg, Fe)O ferropericlase (Fp) is 0.67:0.33 for the lower mantle[21]. We also used this ratio for (Mg, Fe)SiO_3 pPv and Fp in the D″ layer. This means that the anisotropy resulting from pPv LPO should be weakened by approximately two-thirds in the D″ layer assuming isotropy of Fp. The observed polarization anisotropy of the S-wave velocity is ~3% at most[4]. Therefore, pPv in the D″ layer is expected ~4.5% anisotropy to account ~3% anisotropy observed in the D” layer. This requirement is easily satisfied by partial LPO of pPv (Table 2).

Figure 8 summarizes the present idea for seismic anisotropy and LPO structure in the D″ layer. The VTI of the vertical *c* axis and that of the vertical *b* axis can be interpreted as transformation LPO and deformation LPO, respectively. It is noted that isotropic pPv-$MgSiO_3$ is a reasonable interpretation for the seismic feature beneath the Atlantic Ocean; an alternative interpretation may be the VTI of the vertical *a* axis because of less lateral polarization anisotropy than in other cases (Table 2). The difference between beneath the Pacific and Atlantic may be attributed to differences in temperature, chemical composition and strain rate. The proposed LPO behaviour for pPv-$MgSiO_3$ obtained from the

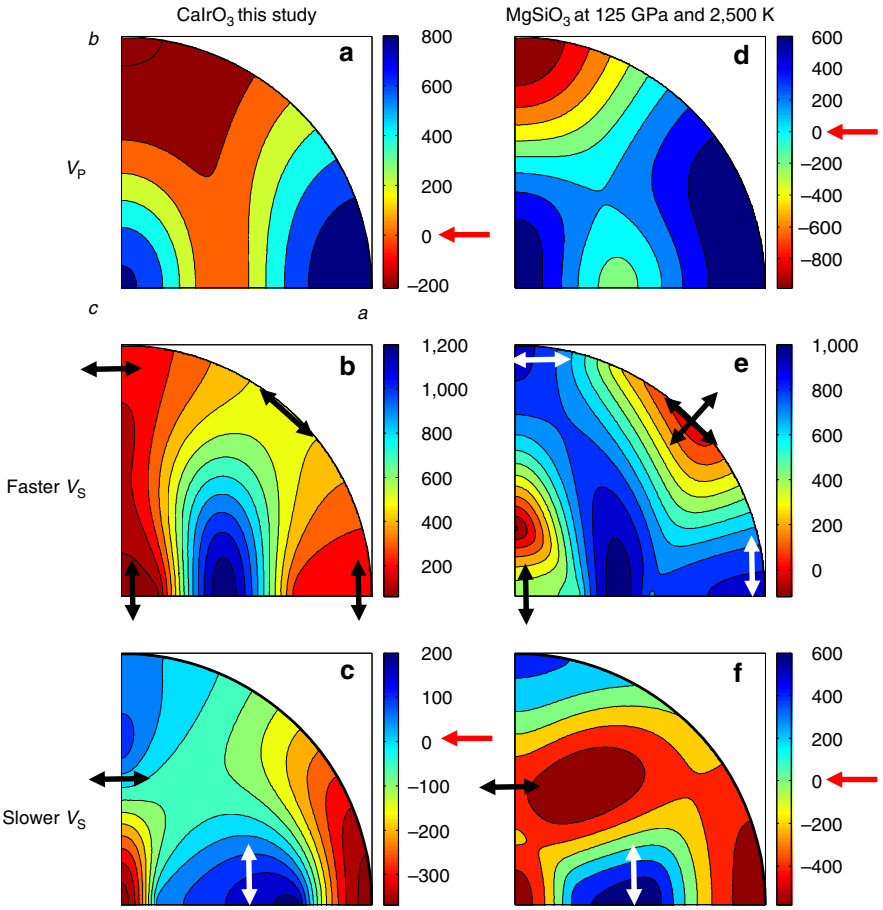

Figure 6 | Velocity difference between anisotropic pPv and isotropic Pv. The left column presents the results for $CaIrO_3$ in the present study, while the right column presents the theoretical calculation for $MgSiO_3$ at 125 GPa and 2,500 K[10]. We recognize common characteristics among the plots for the two materials. Isotropic P-wave velocities of Pv are 5,774 and 13,900 m s^{-1} and S-wave velocities are 2,975 and 7,200 m s^{-1} for $CaIrO_3$ and $MgSiO_3$, respectively. The red arrows beside the scale bars highlight the origin of each scale bar, where the velocities of the two phases are the same. Typical polarizations of the S wave are shown by arrows in the S-wave plots. The crystallographic axes are identical for all plots as shown in plot **a**. In the stereo projections, the propagating waves in the *a*–*b* and *c*–*a* planes are shown along the quarter arc and the bottom edge, respectively. Note that the two polarization arrows in plot **e** between *a* and *b* axes suggest that the two S-wave velocities are nearly the same, as shown in Fig. 7.

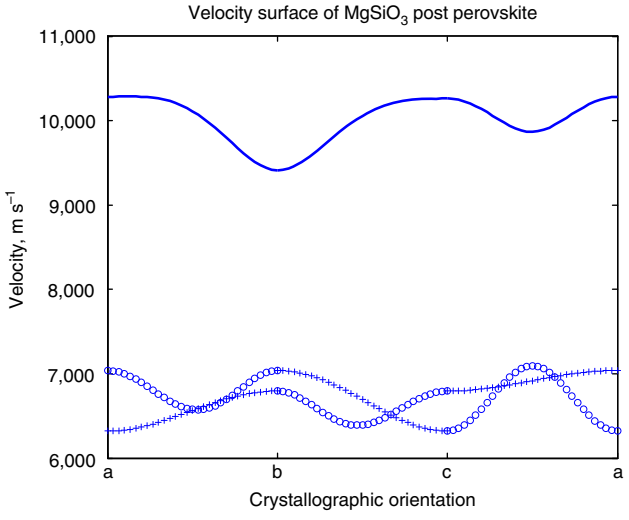

Figure 7 | Velocity surfaces of pPv-$MgSiO_3$ at 125 GPa and 2,500 K. Blue lines are used to specify theoretical results similar to Fig. 2a,b. The upper line is the P-wave velocity and the lower lines are the S-wave velocities. Open circles 'o' and crosses '+' for V_S specify in-plane and out-of-plane particle motions.

present mineral physics perspective is consistent with seismic observation.

To summarize, we presented a new data set of Pv and pPv-$CaIrO_3$ single-crystal elasticity by means of IXS at SPring-8. We used the present results to interpret seismic wave anisotropy in the D″ layer, and proposed a model of pPv LPO in the D″ layer consistent with seismic observations and mineral physics experiments on analogue materials. The present model may allow sophisticated discussion of global mantle convection, which is triggered by heating at the core–mantle boundary and modulated by lateral flow in the D″ layer.

Methods

Measurement of IXS at SPring-8 BL35XU. The small size and black colour of the present samples limit the techniques that can be used to investigate the elastic properties. In particular, the crystal sizes are too small to employ GHz ultrasonic methods[22] or resonant ultrasound spectroscopy[23], where both need crystals larger than 100 μm. In addition, the crystal opacity makes it difficult to apply Brillouin scattering. Therefore, IXS with an X-ray beam diameter of ~70 μm was employed. Each specimen was attached to glass fibres (~100 μm in diameter) using manicure resin and mounted on the four-circle goniometer installed at BL35XU of SPring-8 (ref. 24). The incident X-ray beam energy was 17.794 and 21.747 keV for *Pbnm*-$CaIrO_3$ and *Cmcm*-$CaIrO_3$ measurements, respectively.

The IXS technique[25,26] allows us to determine the elastic properties of a material by measuring the energies of acoustic longitudinal and shear phonon modes. When this information is combined with the precise reciprocal space

Table 2 | Characteristic velocities for crystals of post-perovskite structure.

	V_P, km s^{-1}	V_{SH}, km s^{-1}	V_{SV}, km s^{-1}	V_{SH}/V_{SV}	$\Delta V_S/V_S$
pPv-$CaIrO_3$					
a–*b* plane	6.1 (5)	3.4 (1)	2.8 (2)	1.19	0.11
b–*c* plane	6.1 (4)	3.1 (1)	2.9 (2)	1.06	0.07
c–*a* plane	6.3 (3)	3.4 (6)	3.1 (1)	1.08	0.17
pPv-$MgSiO_3$					
a–*b* plane	14.0 (6)	7.6 (3)	7.1 (3)	1.07	0.09
b–*c* plane	13.9 (6)	7.2 (3)	7.4 (5)	0.98	0.07
c–*a* plane	14.2 (3)	7.4 (6)	7.8 (2)	0.94	0.09

V_P, V_{SH} and V_{SV} are the average velocities of the P wave, SH wave and SV wave, respectively, on each plane specified on the left. ΔV_S is the maximum difference between the SH-wave and SV-wave velocities, and V_S is the average of V_{SH} and V_{SV} on the corresponding plane. The source data for pPv-$CaIrO_3$ and pPv-$MgSiO_3$ are the results of the present IXS study and theoretical computation[10], respectively. The numbers in parentheses correspond to expected uncertainty.

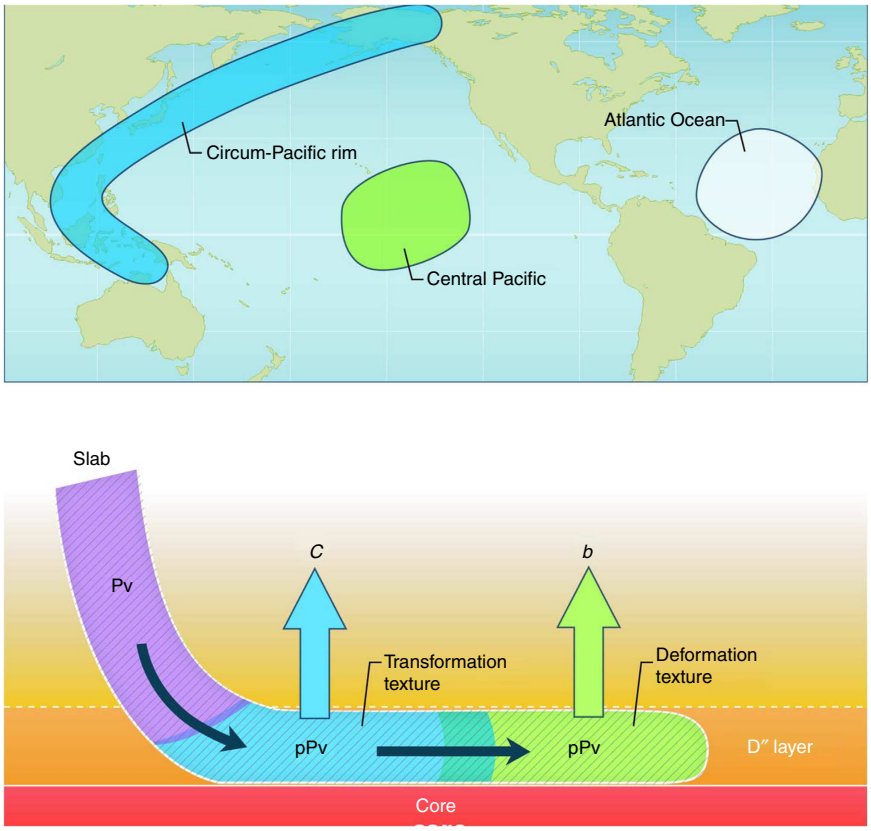

Figure 8 | Schematic illustration of the LPO of pPv-$MgSiO_3$ in the D″ layer. From a mineral physics viewpoint, the Pv slab (purple region) transforms to pPv (light blue region) and the pPv slab then moves along the path of mantle convection with deformation (light-green region). In contrast, from seismic observation, the region of the Circum-Pacific rim has VTI anisotropy of $V_{SH} > V_{SV}$, while the region of the Central Pacific has complicated VTI with any magnitude relation; that is, $V_{SH} > V_{SV}$, $V_{SH} < V_{SV}$ or $V_{SH} \approx V_{SV}$. The region of the Atlantic Ocean (white circle) has VTI with $V_{SH} \approx V_{SV}$, suggesting isotropy or negligible LPO of pPv-$MgSiO_3$. The speculated aligned axes of pPv LPO are shown by arrows for each region; the vertical *c* axis beneath the Circum-Pacific rim and the vertical *b* axis beneath the Central Pacific.

position (momentum transfer) for each measurement, we can determine the sound velocity[27,28]. If measurements are made in many different directions, the velocity information can be combined with the density, allowing all the elastic constants of a material to be determined. In the present work, the two-dimensional, 4×3, analyser array of BL35XU is especially advantageous as it allows access to 12 different directions of momentum transfer simultaneously.

The IXS is applicable on opaque materials; it is the most important advantage of IXS against Brillouin scattering. Further characteristics and procedures of the IXS measurements are summarized in Supplementary Figs 1–5.

Data analysis for elastic constants. A least-squares fit to Christoffel equation was then used to determine the elastic constants[29]. Pv-$CaIrO_3$ and pPv-$CaIrO_3$ have orthorhombic symmetry and thus nine independent elastic constants. The six diagonal elastic constants (C_{11}, C_{22}, C_{33}, C_{44}, C_{55}, C_{66}) is related to nearly independent phonon modes propagating along crystallographic axes, while the three off-diagonal constants (C_{12}, C_{23}, C_{31}) can be determined from combination of a few measurements. We carefully planned the measurement to acquire sufficient data to constrain all nine elastic constants. Using the analyser array, we obtained $\sim$40 and $\sim$60 mode energies for Pv-$CaIrO_3$ and pPv-$CaIrO_3$, respectively.

References

1. Murakami, M., Hirose, K., Kawamura, K., Sata, N. & Ohishi, Y. Post-perovskite phase transition in $MgSiO_3$. *Science* **304,** 855–858 (2004).
2. Oganov, A. R. & Ono, S. Theoretical and experimental evidence for a post-perovskite phase of $MgSiO_3$ in the Earth's D″ layer. *Nature* **430,** 445–448 (2004).

3. Wysession, M. E. *et al.* In *The Core-Mantle Boundary Region, Geodynamics* Vol. 28 (eds Gurnis, M. *et al.*) (American Geophysics Union, 1998).
4. Nowacki, A., Wookley, J. & Kendall, J. M. New advances in using seismic anisotropy, mineral physics and geodynamics to understand deformation in the lowermost mantle. *J. Geodyn.* **52,** 205–228 (2011).
5. Lay, T. & Garnero, E. J. Deep mantle seismic modeling and imaging. *Annu. Rev. Earth Planet. Sci.* **39,** 91–123 (2011).
6. Iitaka, T., Hirose, K., Kawamura, K. & Murakami, M. The elasticity of the $MgSiO_3$ post-perovskite phase in the lowermost mantle. *Nature* **430,** 442–445 (2004).
7. Tsuchiya, T., Tsuchiya, J., Umemoto, K. & Wentzcovitch, R. M. Elasticity of post-perovskite $MgSiO_3$. *Geophys. Res. Lett.* **31,** L14603 (2004).
8. Wookey, J., Stackhouse, S., Kendall, J. M., Brodholt, J. & Price, G. D. Efficacy of the post-perovskite phase as an explanation for lowermost-mantle seismic properties. *Nature* **438,** 1004–1007 (2005).
9. Stackhouse, S., Brodholt, J. P., Wookey, J., Kendall, J. M. & Price, G. D. The effect of temperature on the seismic anisotropy of the perovskite and post-perovskite polymorphs of $MgSiO_3$. *Earth Planet. Sci. Lett.* **230,** 1–10 (2005).
10. Wentzcovitch, R. M., Tsuchiya, T. & Tsuchiya, J. $MgSiO_3$ post perovskite at D" conditions. *PNAS* **103,** 543–546 (2006).
11. Yamazaki, D., Yoshino, T., Ohfuji, H., Ando, J. & Yoneda, A. Origin of seismic anisotropy in the D" layer inferred from shear deformation experiments on post-perovskite phase. *Earth Planet. Sci. Lett.* **252,** 372–378 (2006).
12. Martin, C. D. *et al.* Compression, thermal expansion, structure, and instability of $CaIrO_3$, the structure model of $MgSiO_3$ post-perovskite. *Am. Mineral.* **92,** 1048–1053 (2007).
13. Hunt, S. A. *et al.* Weakening of calcium iridate during its transformation from perovskite to post-perovskite. *Nat. Geosci.* **2,** 794–797 (2009).
14. Hirose, K. & Fujita, Y. Clapeyron slope of the post-perovskite phase transition boundary in $CaIrO_3$. *Geophys. Res. Lett.* **32,** L13313 (2005).
15. McDaniel, C. L. & Schneider, S. J. Phase relations in the CaO-IrO2-Ir system in air. *J. Solid State Chem.* **4,** 275–280 (1972).
16. Sugahara, M. *et al.* Single-crystal X-ray diffraction study at $CaIrO_3$. *Am. Mineral.* **93,** 1148–1152 (2008).
17. Tsuchiya, T. & Tyuchiya, J. Structure and elasticity of Cmcm $CaIrO_3$ and their pressure dependence: Ab initio calculations. *Phys. Rev. B* **76,** 144119 (2007).
18. Niwa, K., Yagi, T. & Ohgushi, K. Elasticity of $CaIrO_3$ with perovskite and post-perovskite structure. *Phys. Chem. Minerals* **38,** 21–31 (2011).
19. Panning, M. & Romanowicz, B. A three-dimensional radially anisotropic model of shear velocity in the whole mantle. *Geophys. J. Int.* **167,** 361–379 (2006).
20. Miyagi, L., Kanitpanyacharoen, W., Stackhouse, S., Militzer, B. & Wenk, H. R. The enigma of post-perovskite anisotropy: deformation versus transformation texture. *Phys. Chem. Minerals* **38,** 665–678 (2011).
21. Jackson, I. Elasticity, composition and temperature of the Earth's lower mantle: a reappraisal. *Geophys. J. Int.* **134,** 291–311 (1998).
22. Chen, G., Spetzler, H. A., Getting, I. C. & Yoneda, A. Cross temperature and pressure derivatives of selected elastic moduli for olivine from GHz ultrasonic interferometry. *J. Geophys. Res.* **101,** 25161–25171 (1996).
23. Yoneda, A., Cooray, T. & Shatskiy, A. Single-crystal elasticity of stishovite: new experimental data obtained using high-frequency resonant ultrasound spectroscopy and a Gingham Check structure model. *Phys. Earth Planet. Inter.* **190-191,** 80–86 (2012).
24. Baron, A. Q. R. *et al.* An X-ray scattering beamline for studying dynamics. *J. Phys. Chem. Solids* **61,** 461–465 (2000).
25. Sette, F. *et al.* Collective dynamics in water by high-energy resolution inelastic X-ray-scattering. *Phys. Rev. Lett* **75,** 850–853 (1995).
26. Burkel, E. Phonon spectroscopy by inelastic x-ray scattering. *Rep. Prog. Phys.* **63,** 171–231 (2000).
27. Bosak, A., Krisch, M., Mohr, M., Maultzsch, J. & Thomson, C. Elasticity of single-crystalline graphite: inelastic x-ray scattering study. *Phys. Rev. B* **75,** 153408 (2007).
28. Lin, J. F., Mao, Z., Yavaş, H., Zhao, J. & Dubrovinsky, L. Shear wave anisotropy of textured hcp-Fe in the Earth's inner core. *Earth Planet. Sci. Lett.* **298,** 361–366 (2010).
29. Fukui, H. *et al.* Precise determination of elastic constants by high-resolution inelastic X-ray scattering. *J. Synchrotron Radiat.* **15,** 618–623 (2008).

Acknowledgements

This work was supported in part by Grants-in-Aid for Scientific Research (Grant No. 22224008 awarded to A.Y.) from the Japan Society for the Promotion of Science. The inelastic X-ray scattering measurement was carried out on the BL35XU at SPring-8 (Proposal Nos. 2011B1425 and 2012A1406).

Author contributions

A.Y. and H.F. planned and managed the present study equally. F.X. prepared sample of *Pbnm*-$CaIrO_3$. A.N. and A. Yoshiasa characterized single-crystal samples. Y.S. and K.O. joined the IXS measurement at SPring-8. S.T., H.U. and A.B. set up the instruments for the IXS measurement. A.Y. wrote the manuscript with input from H.F. and A.B.

Additional information

Supplementary Information accompanies this paper at http://www.nature.com/naturecommunications

Competing financial interests: The authors declare no competing financial interests.

Reprints and permission information is available online at http://npg.nature.com/reprintsandpermissions/

How to cite this article: Yoneda, A. *et al.* Elastic anisotropy of experimental analogues of perovskite and post-perovskite help to interpret D″ diversity. *Nat. Commun.* 5:3453 doi: 10.1038/ncomms4453 (2014).